CrossMark

Aspect-ratio-dependent photoinduced antimicrobial and photocatalytic organic pollutant degradation efficiency of ZnO nanorods

**Rishabh Sharma[1] · Manika Khanuja[2] ·
S. S. Islam[2] · Uma Singhal[3] · Ajit Varma[3]**

Abstract The photo-antimicrobial and photocatalytic performance of ZnO nanorods as a function of aspect ratio are presented. The antibacterial activity of the synthesized ZnO nanorod samples against Gram-negative and Gram-positive bacteria (*Staphylococcus aureus* and *Escherichia coli*, respectively) was determined by shake flask method with respect to time. ZnO nanorods with high aspect ratio showed superior antimicrobial and photocatalytic activity. These results are supported by X-ray diffraction, transmission electron microscopy, scanning electron microscopy, ultraviolet–visible (UV–Vis) spectroscopy, photoluminescence, and Brunauer–Emmett–Teller (BET) studies. Degradation of methylene blue dye as model organic pollutant was used to assess their photocatalytic activity. Pseudo-first-order rate kinetics was used to calculate the photocatalytic reaction rate constant. The mechanisms for both antimicrobial and photocatalytic activity are elucidated.

Keywords ZnO nanorods · Antimicrobial · BET · Photocatalysis · Photoluminescence (PL)

✉ Manika Khanuja
manikakhanuja@gmail.com; mkhanuja@jmi.ac.in

[1] Amity Institute of Nanotechnology, Amity University, Sector-125, Noida, Uttar Pradesh 201303, India

[2] Centre for Nanoscience and Nanotechnology, Jamia Millia Islamia, New Delhi 110025, India

[3] Amity Institute of Microbial Technology, Amity University, Sector-125, Noida, Uttar Pradesh 201303, India

Introduction

Foodborne diseases and water pollution are two primary and challenging global concerns nowadays. According to the Centers for Disease Control and Prevention (CDC), 48 million people get sick and 35,000 die of foodborne diseases each year [1]. Numerous challenges are associated with food safety issues due to changes in food production and supply systems. A new range of bacteria and germs with evolved protection mechanisms along with existing bacteria are continuously evolving, hence the burden of foodborne pathogens remains unknown [2]. The demand for packaged food is now very high, thus the role of the food packaging industry in maintaining quality, safety, and increased shelf-life has become very significant. In this regard, antimicrobial coatings play an active role [3]. Antimicrobial coatings interact with food or headspace to retard growth of microorganisms present on the food surface, leading to longer shelf-life and maintained nutritional value of food. However, newly evolved bacteria have developed protection mechanisms in terms of impermeable cell membranes, thermoresistant endospores, resistance to radiation, desiccation, and denaturing chemicals, and active extrusion of metal ions from the cell, as a result of which present antimicrobial materials are no longer effective against them [4].

Water pollution is the next most important global concern, requiring extensive detoxification based on advanced scientific research. It is well known that the textile industry is mainly responsible for polluting water bodies by simply draining waste primarily containing organic dyes without much-needed and appropriate treatment. ZnO nanorods have been found to resolve this issue based on efficient photocatalysis and mineralization rates. Photocatalysis has potential for use in environmental remediation (pollutant degradation) using a natural source of energy, i.e., sunlight. However, currently available materials fail to utilize the solar spectrum [which consists of 4% UV, 46% visible, and 47% infrared (IR)] effectively due to their wide bandgap. This photocatalytic process involving three steps: (i) generation of electron–hole pairs on irradiation ($h\upsilon > E_\mathrm{g}$), (ii) electron–hole pair separation, and (iii) redox reaction on the surface of nanorods for generation of reactive oxide species (ROS). The reaction of ROS with organic pollutants such as methylene blue (MB) results in degradation of the dye, providing an answer for appropriate degradation of organic dyes in water causing water pollution. Generally, the recombination probability of electron–hole pairs is high, making their separation the rate-limiting step in the photocatalysis process. The rate of electron–hole pair separation depends on the morphology, defect states, and nature of facets of the material used [5, 6].

Therefore, to achieve global benefits, development of novel materials for use in antimicrobial and photocatalytic applications is of significant interest. Recently, nanostructures have emerged as a new class of materials with a wide range of morphologies and tunable physical, chemical, and electronic properties as a function of particle size [6]. ZnO is of particular interest; its bactericidal properties are chiefly due to its photocatalytic activity, as the main mechanism behind its antimicrobial activity is occurrence of ROS on the surface [7, 8]. Catalytically

produced ROS species, i.e., hydroxyl, oxide, and peroxide ions, penetrate the cell membrane, causing subsequent damage to and death of microbial cells.

This antimicrobial activity is a strong function of particle size. In nanostructured materials, owing to their higher surface-to-volume ratio, greater numbers of reactive oxygen species (ROS) are available on the surface, promoting the antimicrobial activity of nanostructured antimicrobial agents such as ZnO nanorods. Additionally, ZnO has been shown to be a prominent candidate as (i) it is "generally recognized as safe" (GRAS) by the US Food and Drug Administration (21CFR182.8991), (ii) it can decompose most water pollutant dyes under UV irradiation, and (iii) among available semiconductor oxides, it offers the widest range of morphologies, including nanorods, nanobelts, and nanoribbons, as reported in various studies [9, 10]. Also, ZnO is favorable as a photocatalyst due to its superior photodegradation efficiency compared with other reported photocatalytic materials such as TiO_2, despite their similar bandgap energy (3.2 eV) [11].

Inspired by these properties of ZnO, in this work, we investigated the effects of the synthesis temperature on the aspect ratio, morphology, surface defects, and optoelectronic properties of ZnO nanorods. We obtained ZnO nanorods with diverse aspect ratios using different synthesis temperatures and found that they exhibited different specific surface area, bandgap, and light absorption properties. These properties are the major factors determining the efficiency of such materials in terms of photocatalysis and antimicrobial activity. So, to study the dependence of the photocatalytic and antimicrobial efficiency on the aspect ratio of the ZnO nanorods, ZnO samples were tested for these applications.

Experimental

Synthesis of ZnO nanorods

ZnO nanorods were prepared by a mechanical-assisted thermal decomposition process [5, 12]. Zinc acetate dihydrate [$Zn(CH_3COO)_2 \cdot 2H_2O$] was used as precursor for synthesis of zinc oxide nanorods. In the synthesis process, zinc acetate dihydrate (2 g) was ground in a mortar and pestle for 45 min then loaded into an alumina crucible, which was then heated in a programmable muffle furnace (at ramp rate of 4 °C/min) at different temperatures (275, 350, 425, and 500 °C) for 4 h to obtain four ZnO nanopowders with different aspect ratios. The obtained powders were then washed twice with distilled water, followed by drying in oven at 80 °C for 8 h.

Characterization

The crystallographic phase of the ZnO samples was determined by X-ray diffraction analysis (Philips PANalytical X'Pert) using Cu K_α X-ray radiation (wavelength $\lambda = 0.15418$ nm). The nanorod structure and surface morphology of the samples were observed using scanning electron microscopy (FEI Quanta 3D FEG) and transmission electron microscopy (FEI Tecnai G2) at accelerating voltage of 20 and

200 kV, respectively. The photoluminescence emission spectra of the ZnO nanorods were recorded at room temperature using a spectrofluorometer (RF 5301 PC, Shimadzu) at excitation wavelength of 325 nm in the scan range of 300–600 nm. The excitation spectra were scanned at step size of 1.0 nm for all samples. The absorption spectrum was measured using a PerkinElmer Lambda 35 UV–Vis spectrometer. Fourier-transform infrared (FTIR) spectra were recorded using a Thermo Scientific Nicolet IS5 model. Pore volumes of the one-dimensional (1D) ZnO nanostructures were determined experimentally by Brunauer–Emmett–Teller (BET) analysis. Nitrogen adsorption–desorption isotherms were measured at 77 K using a volumetric gas adsorption station (NOVA-1000 version 370). To image bacterial cell degradation or degeneration, a scanning electron microscope (EVO 18 Special edition, Zeiss) operated at 5 kV accelerating voltage was used.

SEM analysis of bacterial cells

Sample preparation

The morphological changes in the membrane of bacterial cells (*Staphylococcus aureus* and *Escherichia coli*) were examined before and after treatment with ZnO nanorods. Initially, the bacterial samples were fixed with fixatives (2.5% glutaraldehyde in 0.1 M Na-P buffer, pH 7.4) for 30 min at room temperature, followed by overnight incubation at 4 °C. The samples were then washed with sodium phosphate buffer (0.1 M, pH 7.4) thrice and dehydrated with different ethanol solutions (30, 50, 70, 90, and 100%). The samples were dried at 37°C for about 1 h. Finally, the prepared samples were coated with thin gold film (<10 nm) and observed under SEM at accelerating voltage of 5 kV.

Antimicrobial activity

Preparation and incubation of test organisms

The bacterial species used for the antibacterial assay of ZnO samples were Gram-positive *S. aureus* and Gram-negative *E. coli*. The bacterial cultures were maintained at 37 °C. A single colony of bacteria from each bacterial stock culture (*S. aureus* and *E. coli*) was inoculated in 100 mL sterile Luria–Bertani (LB) broth in a 500-mL Erlenmeyer flask. The prepared bacterial suspensions were then incubated in a shaking incubator at 37 °C.

Antibacterial assay by shake flask test in Luria–Bertani (LB) broth

The antibacterial activity of the zinc oxide nanorods was evaluated as a function of their aspect ratio using the shake flask method with Luria–Bertani (LB) broth, monitoring the growth inhibition by the nanorods with respect to time. Samples containing ZnO nanorods (100 μg/mL) were placed in Erlenmeyer flasks in a shaker incubator at 37 °C under visible-light illumination, and growth was monitored by recording the changes in optical absorbance over fixed intervals of time (0, 2, 4, 6,

and 8 h), followed by a final reading after overnight incubation (24 h), at 600 nm. The antimicrobial efficacy was defined as

$$\frac{(Y - Z)}{Y} \times 100, \tag{1}$$

where Y is the preinoculation bacterial count and Z is the bacterial count after treatment with ZnO nanorods.

Photocatalysis study

For photocatalysis measurements, methylene blue (MB) dye was selected as a model organic contaminant of water released by the textile industry. The photocatalytic activity (degradation efficiency) of the pure ZnO nanorod samples was estimated as a function of their aspect ratio by measuring the degradation rate of MB. The final solution was prepared by mixing 5.0 mg ZnO nanorod powder in 100 mL 10 μM aqueous MB solution, followed by ultrasonication, then stirring in the dark for 2 h to ensure a uniform distribution of nanorods in solution. The solution was then put under illumination, and samples from the solution were collected at regular intervals of 30 min, which were centrifuged and filtered to remove nanorods. The concentration of methylene blue in the collected samples was estimated by UV–Vis spectroscopy. The absorption peak of methylene blue is at 664 nm. The photocatalytic efficiency was calculated using the following formula:

$$\eta = \frac{(C_0 - C)}{C_0} \times 100, \tag{2}$$

where C_0 denotes the initial absorbance of the aqueous MB solution before illumination at $t = 0$ min and C denotes the absorbance of the aqueous MB after adding photocatalyst nanorods and illumination for time t.

Results and discussion

The crystal structure of the as-synthesized ZnO samples was studied by X-ray diffraction (XRD) analysis, as shown in Fig. 1. All four samples (synthesized at 275, 350, 425, and 500 °C) exhibited hexagonal wurtzite structure in agreement with Joint Committee on Powder Diffraction Standards (JCPDS) file number 06-2151. No peak shift or additional peaks were observed, indicating purity of the crystal phase. To understand the effect of the thermal decomposition temperature on the crystal structure, full-width at half-maximum (FWHM) values were calculated for peaks with Miller indices (*hkl*) of (100), (002), and (101), as summarized in Table 1. Although all four samples exhibited pure hexagonal structure, their degree of crystallinity differed. It is observed from Table 1 that, with increasing synthesis temperature, the FWHM values reduced, indicating improved crystallinity [13, 14]. Among all four samples, that annealed at 275 °C was least crystalline, showing the highest FWHM values. This lower crystallinity obtained at low synthesis
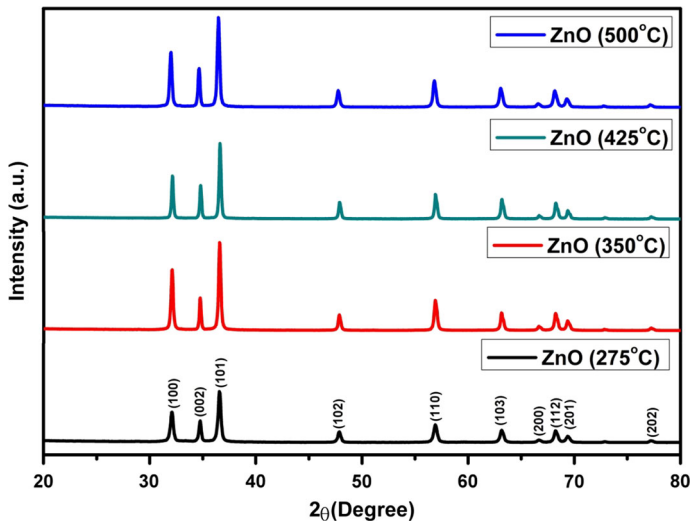
Fig. 1 X-ray diffraction patterns of ZnO samples synthesized at different temperatures

Table 1 FWHM values calculated from XRD peaks for (100), (002), and (101) plane of ZnO samples synthesized at different temperatures

Sample	Plane (100)	Plane (002)	Plane (101)
ZnO (275 °C)	0.421	0.353	0.413
ZnO (350 °C)	0.321	0.277	0.319
ZnO (425 °C)	0.307	0.245	0.309
ZnO (500 °C)	0.244	0.234	0.259

temperature is associated with a larger number of surface defects [15]. Surface defects act as active sites for photoreactions [16] and introduce an intermediate energy band in ZnO, which reduces the photon energy required for electron transition between conduction and valence band, thus enhancing its photosensitivity [5]. So, surface defects are beneficial for improving the photoassisted antimicrobial and photocatalytic performance.

To understand the effect of the synthesis temperature on the ZnO morphology, we performed scanning electron microscopy (SEM) on all the samples (Fig. 2). The sample synthesized at 275 °C (Fig. 2a) exhibited perfect nanorod-like morphology with high aspect ratio of 18.75. On increasing the synthesis temperature, reduction of the length of the rods was seen (Fig. 2b, c), with complete loss of the rod-like morphology at 500 °C (Fig. 2d). Table 2 presents the average length, width, and aspect ratio of ZnO for each sample. There is a well-defined space-charge region in 1D nanorod structures, which limits the flow of electrons to only the direction along their length, resulting in their increased delocalization [16]. This delocalization of electron–hole pairs due to the nanorod morphology hugely suppresses electron–hole
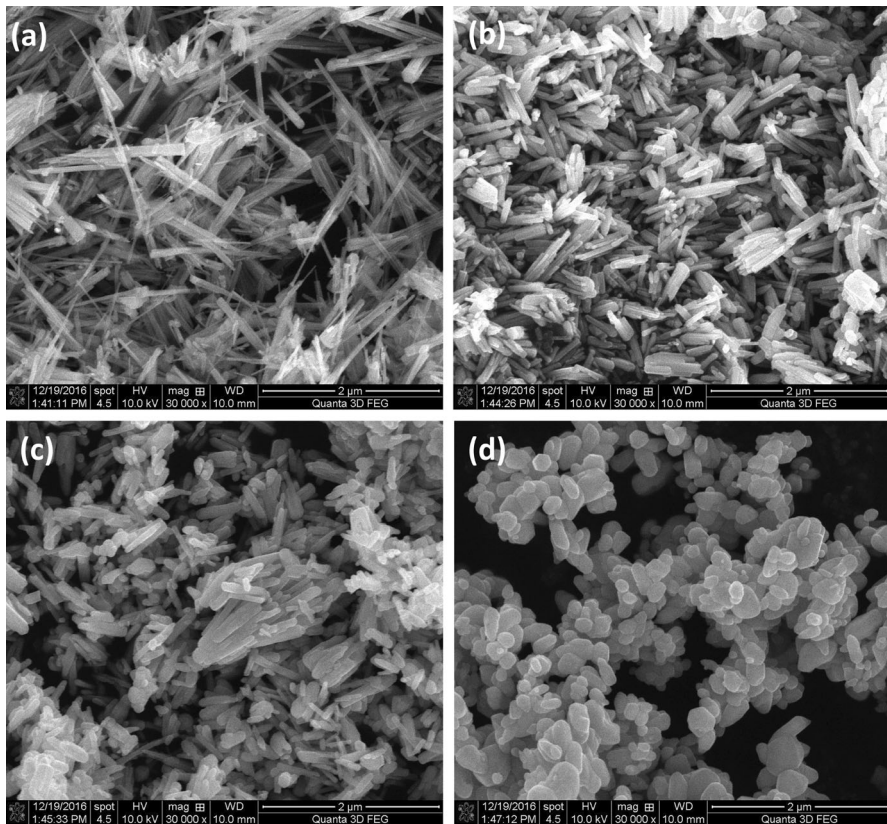
Fig. 2 Scanning electron micrographs of **a** ZnO (275 °C), **b** ZnO (350 °C), **c** ZnO (425 °C), and **d** ZnO (500 °C)

Table 2 Average length, average width, and aspect ratio of ZnO samples observed from SEM images

Sample	Average length	Average width	Aspect ratio
ZnO (275 °C)	1.5 μm	80 nm	18.75
ZnO (350 °C)	510 nm	75 nm	6.8
ZnO (425 °C)	360 nm	85 nm	4.23
ZnO (500 °C)	240 nm	–	–

recombination, which is beneficial for improving the photocatalytic and photo-antimicrobial performance. Figure 3 shows TEM micrographs of ZnO samples synthesized at temperature of 275, 350, 425, and 500 °C. These TEM images also confirm the nanorod morphology of the ZnO sample prepared at temperature of 275 °C. The reduction in the aspect ratio on increasing the synthesis temperature from 275 to 500 °C is also clearly evident from these TEM images, in good agreement with the SEM micrographs in Fig. 2.
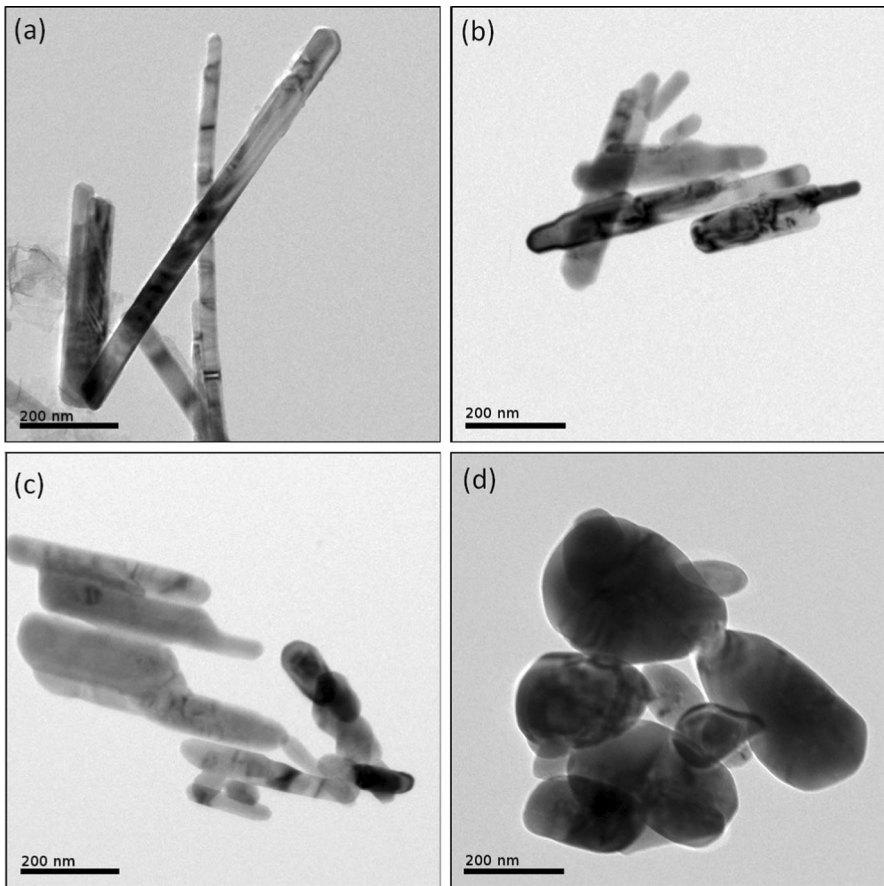
Fig. 3 Transmission electron micrographs of **a** ZnO (275 °C), **b** ZnO (350 °C), **c** ZnO (425 °C), and **d** ZnO (500 °C)

Figure 4a shows the photoluminescence band of all the ZnO samples. The photoluminescence of ZnO includes two bands: the first is a near-band-edge (NBE) emission band or ultraviolet (UV) band, while the second is a broad visible emission band or defect-level (DL) band. The peak intensity decreased with increasing aspect ratio. This is due to the presence of a greater number of surface defects, which act as nonradiative recombination trapping centers, thus increasing surface recombination and hence decreasing the PL intensity. So, from the PL spectra, it can be inferred that the lowest PL intensity of the ZnO sample synthesized at 275 °C is due to its maximum number of surface defects.

The PL spectra are highly asymmetric, indicating that it has many origins. Figure 4b shows the PL spectra of all the samples fit using Gaussian components. The peak at ∼ 385 nm corresponds to near-band-edge (NBE) emission, being the characteristic emission of ZnO. The peak observed at ∼ 403 nm is designated as UV emission arising due to singly ionized oxygen vacancies, while the peaks observed
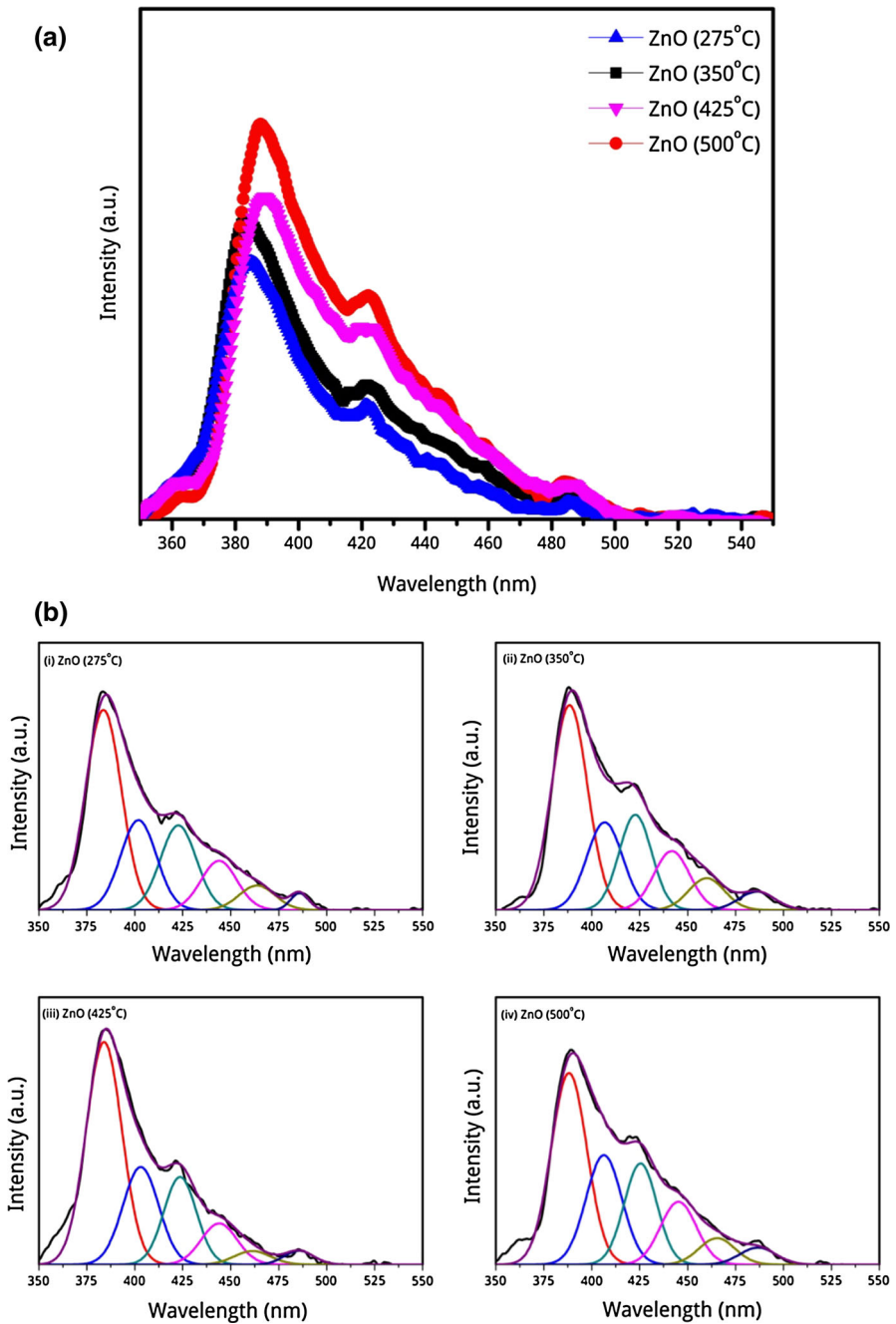
Fig. 4 **a** PL spectra of ZnO samples, **b** Gaussian-fit PL spectra of ZnO samples

at ~424 nm and ~445 are attributed to Zn_i and Zn_i^{+1} interstitial zinc donor defects, respectively. The peak observed at ~462 nm is due to doubly ionized zinc vacancy (V_{Zn}^{2-}), and the peak observed at ~486 nm is attributed to recombination of shallow trapped electron with acceptor levels above the valence band [17].

The BET surface area of all the samples, i.e., (a) ZnO (275 °C), (b) ZnO (350 °C), (c) ZnO (425 °C), and (d) ZnO (550 °C), was investigated using nitrogen adsorption–desorption isotherms (Fig. 5). Before each measurement, the sample was degassed at temperature of 250 °C for 12 h. The N_2 adsorption–desorption isotherms of the ZnO samples were found to be of type II, as per the Brunauer–Dening–Dening–Teller (BDDT) classification [18]. All samples exhibited the highest adsorption at relative pressures P/P_0 close to 1.0, suggesting presence of large macropores. The specific surface area of the ZnO samples synthesized at temperature of 275, 350, 425, and 550 °C was found to be 30.031, 14.058, 12.101, and 4.429 m^2/g, respectively. Thus, the specific surface area decreased with increasing synthesis temperature, consistent with the aspect ratio of the ZnO samples. The BET analysis results confirmed that the ZnO sample synthesized at 275 °C had the highest surface area, leading to the maximum number of surface sites available for photoreactions to take place, hence enhancing the rate of photocatalysis and the photoassisted antimicrobial performance.
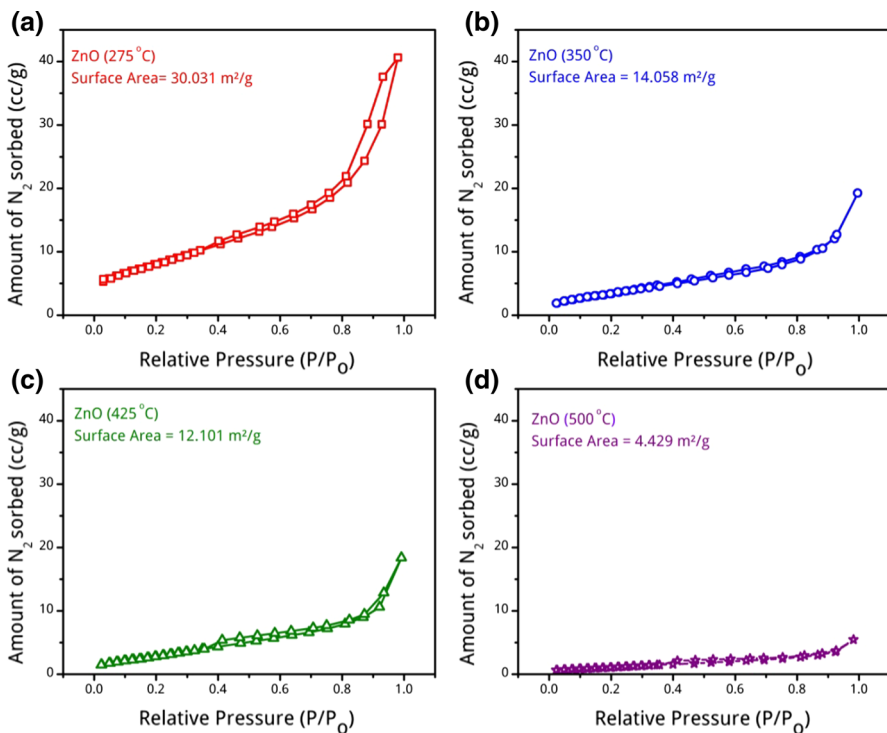

Fig. 5 Nitrogen adsorption–desorption isotherms of **a** ZnO (275 °C), **b** ZnO (350 °C), **c** ZnO (425 °C), and **d** ZnO (500 °C)
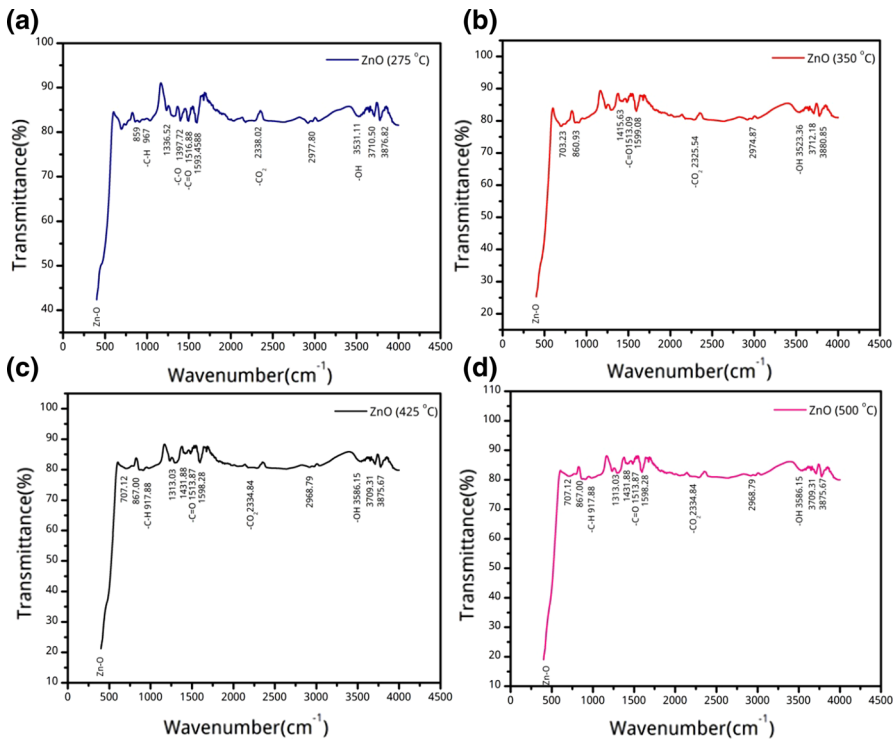
Fig. 6 FTIR spectra of **a** ZnO (275 °C), **b** ZnO (350 °C), **c** ZnO (425 °C), and **d** ZnO (500 °C)

The FTIR spectra (Fig. 6) clearly show the ZnO absorption band in the region from 400 and 600 cm^{-1}. The IR spectrum of ZnO usually shows a characteristic absorption band between 420 and 510 cm^{-1} due to two transverse optical stretching modes of ZnO [19]. The spectra showed bands at 713 and 844 cm^{-1} corresponding to C–H stretching of alkanes, C–H (aromatics), CQC–H (alkynes), and –OH stretching of intramolecular H-bond, CQO, and C–C stretching of alkanes. The peak at ~ 940 cm^{-1} can be attributed to aromatic C=C stretching mode, while the peak at 1061 cm^{-1} is due to alcohols, acetate, ethers, and carboxyl compounds. Additional absorption bands at 1590, 1415, and 1340 cm^{-1} were ascribed to organic impurities originating from reaction intermediates, which can be identified as Zn hydroxo acetate complex or tetranuclear oxo zinc acetate cluster [Zn$_4$O(CH$_3$COO)$_6$]. The bands at 2987 and 3197 cm^{-1} correspond to amide linkage between amino acid residues in the proteins, stretching vibrations of amide II, and presence of atmospheric CO$_2$. The absorption band at ~ 3425 cm^{-1} arises due to stretching mode of O–H group, revealing the presence of a small amount of water absorbed by the ZnO nanostructure [5, 19].
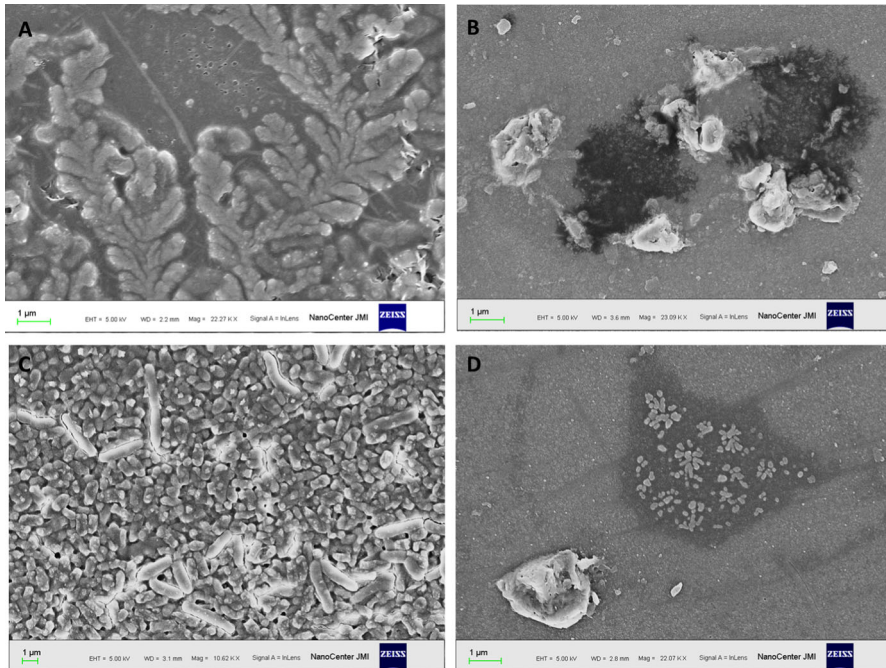
Fig. 7 SEM micrographs of control **a** *E. coli* and **b** *S. aureus*, and **c** *E. coli* and **d** *S. aureus* in presence of ZnO (275 °C) nanorods

Antimicrobial activity

Figure 7 shows SEM micrographs of (A) *E. coli* control, (B) *S. aureus* control, and (C, D) *E. coli* and *S. aureus* treated with ZnO (275 °C), respectively. The SEM images in Fig. 7a, b show *E. coli* and *S. aureus* bacterial cells of normal size with intact intercellular structure and well-maintained intercellular content. On the contrary, Fig. 7c, d shows distorted cell membranes with leakage of intercellular content from the cells in presence of ZnO (275 °C); the resulting null cells finally aggregated to form dead colonies, as depicted in these SEM micrographs.

Figure 8 shows the antimicrobial activity of the ZnO nanorods against *S. aureus* and *E. coli* bacteria for different times and as a function of the ZnO nanorod aspect ratio (for samples prepared at 275, 350, 425, and 500 °C). Table 3 summarizes the antimicrobial activity of the ZnO nanorods as a function of their aspect ratio and time. When the ZnO nanorod samples were excited with energy $h\upsilon > E_g$, electron–hole (e^- and h^+) pairs were generated in the conduction band (E_c) and valence band (E_v), respectively, as shown in Fig. 9. An electron (e^-) in the conduction band can interact with molecular oxygen (O_2) to form a superoxide anion (O_2^-), while the hole in the valence band can interact with a hydroxide ion (OH^-) to form a hydroxide radical ($OH^.$). Together, the O_2^- and $OH^.$ radicals are called a reactive oxide species (ROS), being principally responsible for the antimicrobial activity. Researchers have reported that the main mechanism underlying the antimicrobial activity of ZnO
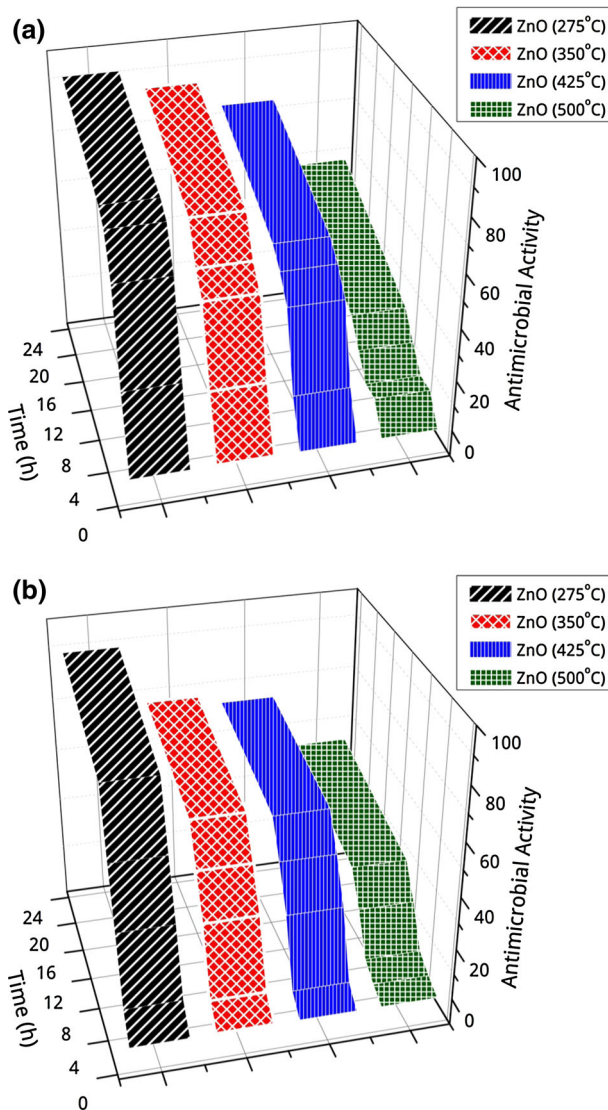
Fig. 8 Antimicrobial efficacy of different ZnO samples against **a** *E. coli* and **b** *S. aureus*

is ROS generation on the surface [7, 8]. The ROS species first rupture the cell wall, followed by its decomposition leading to leakage of minerals, proteins, and genetic material, causing cell death. Researchers have also proposed contact killing as a plausible mechanism to explain the antimicrobial activity of ZnO [20]. ZnO (275 °C) showed better antimicrobial activity compared with the other samples, for both Gram-positive as well as Gram-negative bacteria, owing to its highest surface area, as confirmed by the BET results. The higher antimicrobial activity of ZnO (275 °C) is attributed to (i) its lower charge recombination rate, (ii) its large surface

Table 3 Antimicrobial activity of ZnO samples against (a) *E. coli* and (b) *S. aureus*

Time	ZnO (275 °C)	ZnO (350 °C)	ZnO (425 °C)	ZnO (500 °C)
(a) *E. coli*				
0	0	0	0	0
2	27.38516	22.61484	15.72438	9.71731
4	61.17788	50.60096	43.99038	9.49519
6	75.34884	57.32558	52.09302	17.2093
8	79.05702	70.72368	57.34649	25.65789
24	91.7886	84.79675	74.84553	47.56098
(b) *S. aureus*				
0	0	0	0	0
2	8.45987	6.50759	5.20607	2.81996
4	31.72757	30.39867	28.90365	6.74419
6	51.96078	44.81793	43.83754	20.7563
8	75.82668	58.60889	55.98632	32.02166
24	88.91089	67.12871	63.44554	42.79208

area, resulting in a higher number of ROS species on the surface, and (iii) its abrasive surface texture, due to the greater number of surface defects (as confirmed by PL studies), edges, and corners. Higher surface roughness contributes to mechanical damage to the cell membrane [20], leading to increased membrane permeability for entry of ZnO nanorods. Additionally, membrane deformation causes changes in protein levels, ultimately leading to inhibition of cellular metabolism and cell death [20–23]. Thus, the higher the aspect ratio of the nanorods, the greater the amount of ROS species that is available for membrane penetration, and contact killing is also more pronounced, as more ZnO species are in contact with the bacterial cell.

Photocatalysis

Photocatalytic action, also known as an advanced oxidation process (AOP), has lower power consumption and is easy to control. Also, photocatalytic processes do not produce secondary pollution. When incident radiation ($hv > E_g$) illuminates a photocatalyst, electrons migrate from the valence band (VB) to conduction band (CB), and holes are formed in the valence band. The efficiency of the photocatalyst depends on the number of OH⁻ and O⁻ radicals generated, as these are powerful agents for oxidization of dyes. These radicals react with the dye molecule and abstract an electron from it, thereby commencing the photodegradation process [5, 24, 25].

The photocatalytic degradation efficiency of the samples was tested using methylene blue under illumination for different time intervals (0, 15, 30, 45, and 60 min). Figure 9 shows the C/C_0 versus time plot for all four samples, revealing
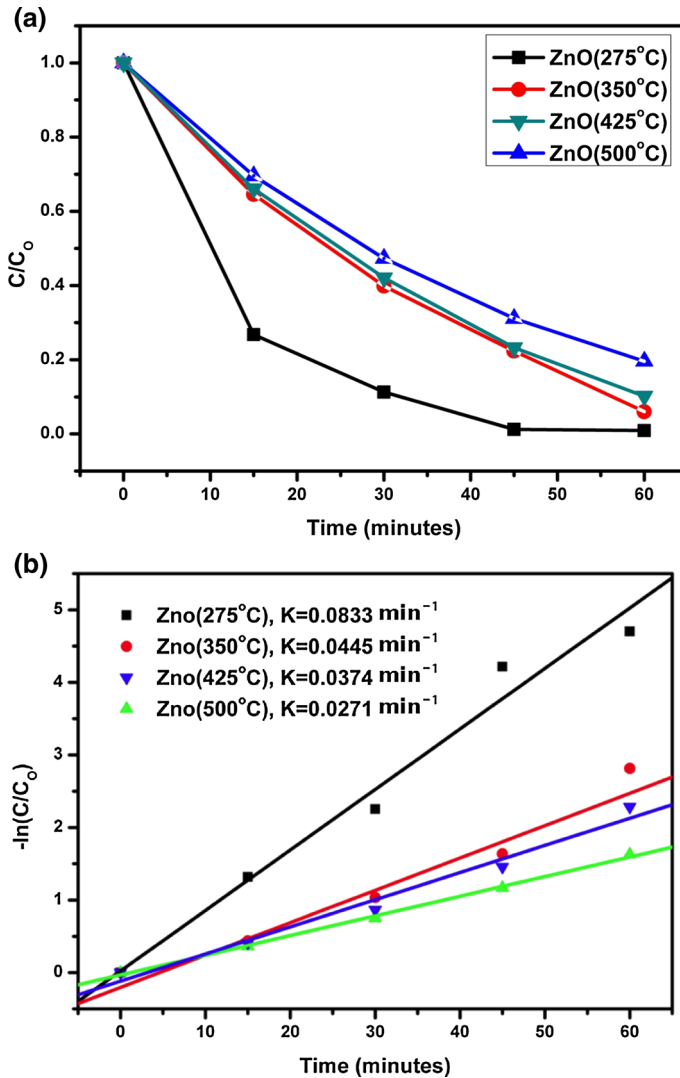
Fig. 9 Photocatalytic dye degradation: **a** C/C_0 versus time, **b** first-order kinetics of photodegradation of methylene blue by ZnO samples as photocatalyst

maximum dye degradation with respect to time for the ZnO (275 °C) sample, with 100% dye degradation in 45 min.

Photocatalytic dye degradation follows pseudo-first-order kinetics, as described by the following equation [5, 24, 25]:

$$C = C_0 e^{-kt} \tag{3}$$

or

$$-\ln\left(\frac{C}{C_0}\right) = -kt, \qquad (4)$$

where k is the rate constant of the pseudo-first-order reaction. The rate constant for dye degradation was therefore calculated as the slope of the $-\ln\left(\frac{C}{C_0}\right)$ versus time plot. Figure 10 shows the pseudo-first-order kinetics plot for dye degradation by all the ZnO samples. The rate constant for the ZnO samples synthesized at 275, 350, 425, and 500 °C was found to be 0.0833, 0.0445, 0.0374, and 0.0271 min^{-1}, respectively. The higher the rate constant, the faster the reaction rate. It is clearly implied by these data that the sample prepared at 275 °C showed the maximum rate constant and hence the fastest dye degradation.

UV–Vis spectroscopy was performed on the samples to measure the band-edge absorption and the change in its value with respect to the synthesis temperature. Figure 10 shows the UV–Vis absorption spectrum of all the samples, with the absorption peak for ZnO synthesized at temperature of 275 °C lying at 371 nm. Red-shift in the absorption peak was observed on increasing the temperature, reaching 381 nm for ZnO (500 °C), equivalent to that of bulk ZnO [26]. A Tauc plot for each sample was obtained by plotting $(\alpha h v)^n$ versus $(h v)$ [18, 27, 28] (Fig. 11), where α is the absorption coefficient, v is the frequency, and h is Planck's constant. The bandgap was calculated by drawing the intercept on each Tauc plot, yielding values of 3.18, 3.14, 3.12 and 3.10 eV for ZnO synthesized at 275, 350, 425, and 500 °C, respectively. The higher the bandgap energy, the greater the photon energy required to excite electrons from the valence to conduction band, hence the lower the photosensitivity.
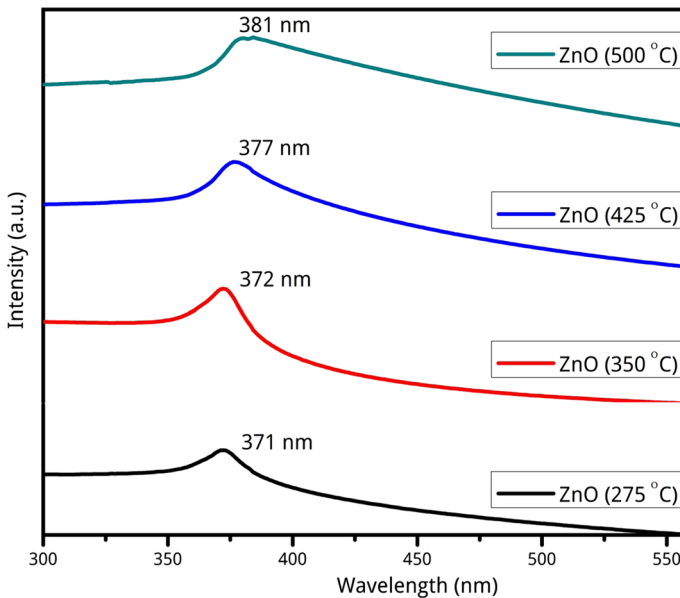

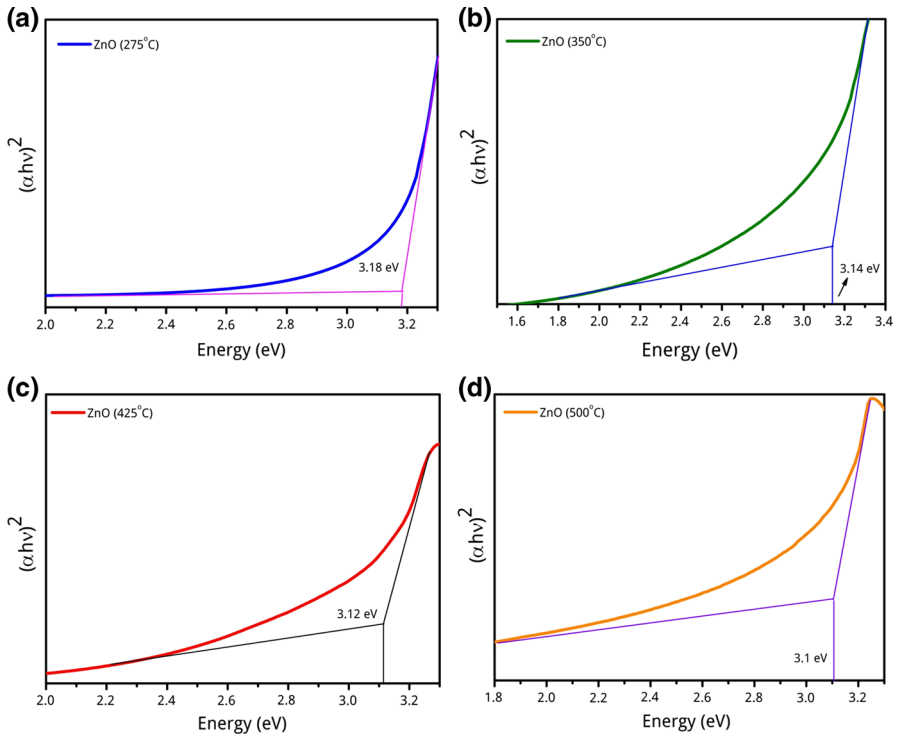**Fig. 10** UV–Vis spectra of ZnO samples

Fig. 11 Tauc plot for **a** ZnO (275 °C), **b** ZnO (350 °C), **c** ZnO (425 °C), and **d** ZnO (500 °C)

According to the UV–Vis spectra, ZnO synthesized at 275 °C seems to be the most light insensitive among all four samples, but it showed the best photocatalytic and photoassisted antimicrobial performance. The contradiction between these results can be explained based on the formation of an intermediate band in ZnO due to defect bands. An intermediate defect band was formed in all four samples, as confirmed by PL. This intermediate band acts as a light sensitizer by increasing the number of steps in electron transition from the valence to conduction band. An electron jumps from the valence to intermediate band and from the intermediate to conduction band, leading to a reduction in the photon energy required for the transition [29]. So, due to the presence of the intermediate band in ZnO (275 °C), its slightly higher bandgap energy (3.18 eV) had no effect on its photosensitivity.

The fundamental or molecular bandgap is the difference between the ionization energy and electron affinity, whereas the optical band is the excitation energy from the highest ground state to lowest excited state [30]. In the optical band transition, electrostatic binding exists between electrons and holes in the lowest excited state. Due to this binding energy, the optical bandgap is always lower than the fundamental bandgap, and the difference between the fundamental and optical bandgaps is equal to the binding energy between electrons and holes in the excited state. The fundamental bandgap of bulk ZnO is 3.4 eV [31], whereas the optical bandgap was 3.10–3.18 eV for all four of our samples.
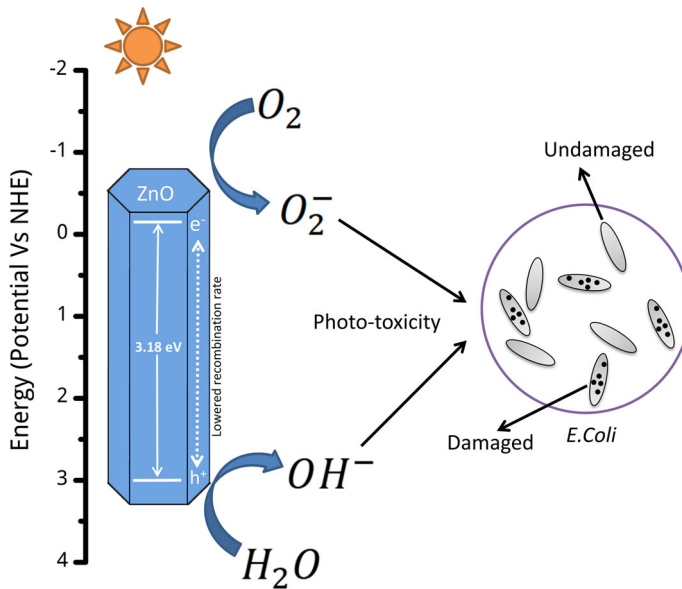
Fig. 12 Mechanism of photoinduced antimicrobial activity of ZnO nanorods against *E. coli* bacteria

The high photocatalytic and photoassisted antimicrobial performance of the ZnO sample prepared at 275 °C are mainly due to two reasons: firstly, its high aspect ratio with perfect nanorod structure compared with the other samples synthesized at higher temperatures; and secondly, the presence of a large number of surface defects, resulting in intermediate defect bands in ZnO. In addition, it is due to the large surface area. As discussed above, the high aspect ratio of the ZnO synthesized at 275 °C offers the advantage of low recombination rate of charge carriers, thus increasing the number of photoexcited electrons and holes available for photoreactions. Large surface area is beneficial for enhancing photoreactions by increasing the number of photoassisted reactions taking place per unit area of catalyst surface. Also, the intermediate band formed by defects reduces the photon energy required for electron transition between valence and conduction band, thus enhancing the photosensitivity. Figure 12 shows a schematic of the photo-induced antimicrobial action of ZnO nanorods against *E. coli* bacterium. Generation of ROS species (O_2^- and OH^-) on exposing the nanorods to visible light is responsible for the degradation of the bacterial cell membranes, resulting in their death. Also, as discussed in detail in the antimicrobial activity section (Sect. 4.1), the rough surface of these rods also causes mechanical damage to the cell walls.

Conclusions

The antimicrobial activity and photocatalytic degradation efficiency of ZnO nanorods were studied as functions of the synthesis temperature, which in turn controls the aspect ratio, of the nanorods. ZnO nanorods synthesized at 275 °C

showed the highest aspect ratio as well as better photo-antimicrobial and photocatalytic activity due to (i) their large surface area, as confirmed by BET study, resulting in a greater number of reactive oxide species (ROS) on the surface; (ii) increased spatial confinement of e^- and h^+; (iii) the large number of surface defects, leading to increased photon absorption. The present results demonstrate that ZnO nanorods with high aspect ratio have potential as an effective antimicrobial agent against Gram-positive as well as Gram-negative bacteria and as a photocatalytic agent against organic pollutants such as MB. Thus, ZnO nanorods have a wide range of applications in (i) food packaging industry, (ii) sterilization of equipment in hospitals that are contaminated with microorganisms such as bacteria and fungi, (iii) water purification involving inactivation of pathogens (antimicrobial), and (iv) degradation of organic dyes (photocatalysis), the main water pollutants released by the textile industry.

References

1. CDC, Estimates of Foodborne Illness in the United States (2016)
2. D.G. Newell, M. Koopmans, L. Verhoef, E. Duizer, A. Aidara-Kane, H. Sprong, M. Opsteegh, M. Langelaar, J. Threfall, F. Scheutz, J. van der Giessen, H. Kruse, Int. J. Food Microbiol. **145**, 493 (2011)
3. S.-Y. Sung, L.T. Sin, T.-T. Tee, S.-T. Bee, A.R. Rahmat, W.A.W.A. Rahman, A.-C. Tan, M. Vikhraman, Trends Food Sci. Technol. **33**, 110 (2013)
4. Y. Xie, Y. He, P.L. Irwin, T. Jin, X. Shi, Appl. Environ. Microbiol. **77**, 2325 (2011)
5. T. Bhuyan, M. Khanuja, R. Sharma, S. Patel, M.R. Reddy, S. Anand, A. Varma, J. Nanoparticle Res. **17**, 1 (2015)
6. D. Koziej, A. Lauria, M. Niederberger, ChemInform **45**, 14 (2014)
7. M. Shoeb, B.R. Singh, J.A. Khan, W. Khan, B.N. Singh, H.B. Singh, A.H. Naqvi, Adv. Nat. Sci. Nanosci. Nanotechnol. **4**, 35015 (2013)
8. T. Gordon, B. Perlstein, O. Houbara, I. Felner, E. Banin, S. Margel, Colloids Surf. A Physicochem. Eng. Asp. **374**, 1 (2011)
9. N. Kislov, J. Lahiri, H. Verma, D.Y. Goswami, E. Stefanakos, M. Batzill, Langmuir **25**, 3310 (2009)
10. Y. Kozuka, A. Tsukazaki, M. Kawasaki, Appl. Phys. Rev. **1**, 011303 (2014)
11. R. Ullah, J. Dutta, J. Hazard. Mater. **156**, 194 (2008)
12. N. Shakti, A. Prakash, T. Mandal, M. Katiyar, Mater. Sci. Semicond. Process. **20**, 55 (2014)
13. S. Dhall, N. Jaggi, R. Nathawat, Sens. Actuators A Phys. **201**, 321 (2013)
14. H.J. Kim, M.K. Joshi, H.R. Pant, J.H. Kim, E. Lee, C.S. Kim, Colloids Surf. A Physicochem. Eng. Asp. **469**, 256 (2015)
15. D. Chen, Z. Wang, T. Ren, H. Ding, W. Yao, R. Zong, Y. Zhu, J. Phys. Chem. C **118**, 15300 (2014)
16. X. Zhang, J. Qin, Y. Xue, P. Yu, B. Zhang, L. Wang, R. Liu, Sci. Rep. **4**, 4596 (2014)
17. A. Baral, M. Khanuja, S.S. Islam, R. Sharma, B.R. Mehta, J. Lumin. **183**, 383 (2017)
18. K.S.W. Singh, D.H. Everett, R.A.W. Haul, L. Moscou, R.A. Pierotti, J. Rouquerol, T. Siemieniewska, Pure Appl. Chem. **57**, 603–619 (1985)
19. D.P. Ojha, M.K. Joshi, H.J. Kim, Ceram. Int. **43**, 1290 (2017)
20. Y. Jiang, J. Gang, S.-Y. Xu, Nano-Micro Lett. **4**, 228 (2012)
21. P. J. P. Espitia, de N. F. F. Soares, J. dos S. R. Coimbra, N. J. de Andrade, R. S. Cruz, E. A. A. Medeiros, Food Bioprocess Technol. **5**, 1447 (2012)
22. K. Hirota, M. Sugimoto, M. Kato, K. Tsukagoshi, T. Tanigawa, H. Sugimoto, Ceram. Int. **36**, 497 (2010)
23. R.J.V. Michael, B. Sambandam, T. Muthukumar, M.J. Umapathy, P.T. Manoharan, Phys. Chem. Chem. Phys. **16**, 8541 (2014)

24. S. Singh, R. Sharma, G. Joshi, J.K. Pandey, Korean J. Chem. Eng. **1**, 1 (2016)
25. R. Sharma, Uma, S. Singh, A. Verma, M. Khanuja, J. Photochem. Photobiol. B Biol. **17**, 288 (2016)
26. J. Liu, J. Cao, Z. Li, G. Ji, M. Zheng, Mater. Lett. **61**, 4409 (2007)
27. T. Bhuyan, K. Mishra, M. Khanuja, R. Prasad, A. Varma, Mater. Sci. Semicond. Process. **32**, 55 (2015)
28. S. Singh, R. Pendurthi, M. Khanuja, S. Chauhan, Appl. Phys. A, doi:10.1007/s00339-017-0806-8
29. A. Leelavathi, G. Madras, N. Ravishankar, Phys. Chem. Chem. Phys. **15**, 10795 (2013)
30. J.-L. Bredas, Mater. Horiz. **1**, 17 (2014)
31. C.L. Dong, C. Persson, L. Vayssieres, A. Augustsson, T. Schmitt, M. Mattesini, R. Ahuja, C.L. Chang, J.-H. Guo, Phys. Rev. B **70**, 195325 (2004)